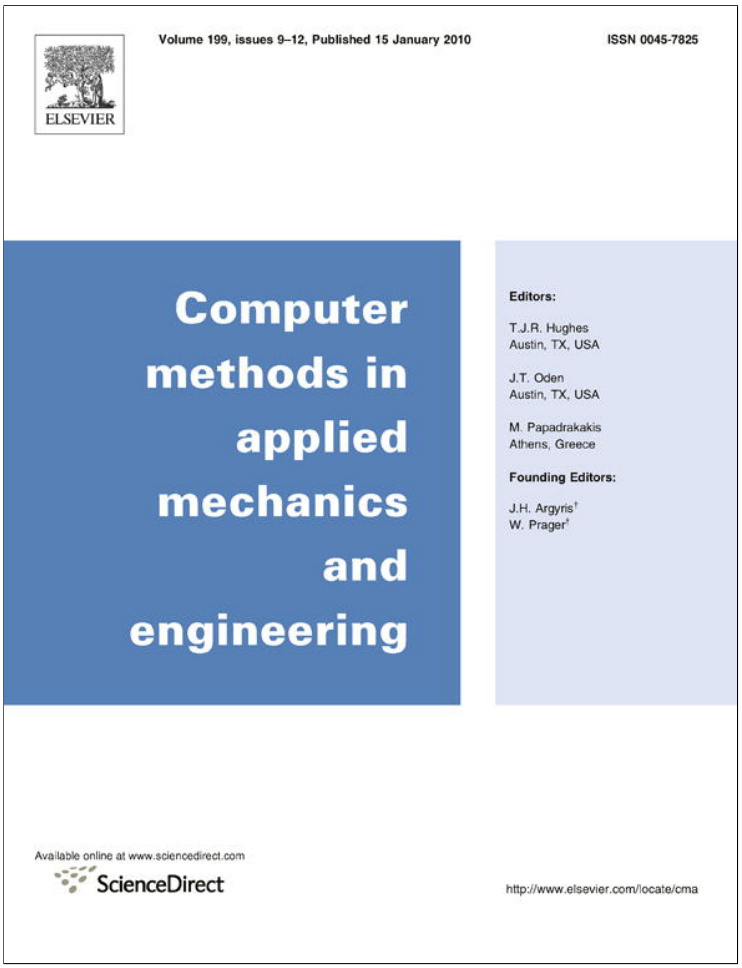

Comput. Methods Appl. Mech. Engrg. 199 (2010) 547–556

Contents lists available at ScienceDirect

Comput. Methods Appl. Mech. Engrg.

journal homepage: www.elsevier.com/locate/cma

A multiscale cohesive zone model and simulations of fractures

Xiaowei Zeng, Shaofan Li *

Department of Civil and Environmental Engineering, University of California, 783 Davis Hall, Berkeley, CA 94720, USA

ARTICLE INFO

Article history:
Received 27 May 2009
Received in revised form 1 September 2009
Accepted 17 October 2009
Available online 28 October 2009

Keywords:
Atomistic simulation
Cohesive zone model
Crack propagation
Finite element method
Impacts
Multiscale simulations

ABSTRACT

In this work, a novel multiscale cohesive zone model is proposed, in which the bulk material is modeled as a local quasi-continuum medium that obeys the Cauchy–Born rule while the cohesive force and displacement relations inside the cohesive zone are governed by a *coarse grained depletion potential*. The interface depletion potential is constructed based on the Derjaguin approximation of nonlocal colloidal interactions. By doing so, the interface constitutive descriptions are made genetically consistent with the bulk constitutive relations that are enriched from underneath atomistic structure. The method provides an effective means to describe properties of material inhomogeneities such as grain boundaries, bi-material interfaces, slip lines, and inclusions, etc. We have developed and implemented the proposed multiscale cohesive zone model in a cohesive finite element weak Galerkin formulation, and we have applied it to simulate dynamic fracture problems in solids. The numerical simulation results have shown that the method has successfully captured the phenomenon of spall fracture during simulations of impacts and penetrations.

1. Introduction

The theory of cohesive zone model may be traced back to the early works by Dugdale [7] and Barrenblatt [2], in which both concepts of atomistic de-cohesion and the defect process zone are established. Xu and Needleman [27] first related the cohesive zone model with finite element (FE) analysis, and they developed the cohesive finite element method and successfully applied it to simulate dynamic fracture problems. Since then, the phenomenological cohesive zone model has gained much popularity in material failure simulations, and it has been extensively applied to solve engineering fracture mechanics problems e.g. Ortiz and Pandolfi [19]. However, so far most of these applications are macroscale material failure analysis, and they may be restricted to the small scale yielding conditions. In other words, the method is most suitable for simulations of brittle fractures or quasi-brittle fractures. When the crack size becomes very small, say below sub-micron scale, the conventional cohesive zone model may reach to its limit, because irreversible plasticity theory is highly size-dependent, and the conventional cohesive law inside the cohesive zone may become inaccurate. Another drawback is that in conventional cohesive finite element method, the bulk and interface constitutive relations are disjointed; and in conventional cohesive FEM the normal and tangential cohesive potential laws are also prescribed separately, even though recently attempts have been made to develop a mix-mode universal phenomenological cohesive potential, e.g. Park et al. [20].

To advance the current cohesive finite element technology, an ideal cohesive finite element paradigm would be based on the interface cohesive potential that can be linked to the atomistic potential obtained from first-principle calculations. This fundamental approach is considered as the ultimately replacement to the empirical cohesive potential approach, see Nguyen and Ortiz [18], Braides et al. [3], and Liu et al. [14]. Pursuing this goal, both Nguyen and Ortiz [18] and Braides [3] have investigated this problem by using formal asymptotics and renormalization group techniques to obtain a coarse grained or effective cohesive potential for interfacial cohesive zone.

In this work, by taking a completely different approach, we first consider the cohesive zone as a finite width zone, and then we propose to use the coarse graining methodology in colloidal physics to model constitutive relations in the interplanar cohesive zone. By assuming that the cohesive zone is a relatively "soft" interface zone, one may derive a so-called depletion for the interface zone by using Derjaguin's approximation (see Derjaguin [6]). Second we use the Cauchy–Born rule to model the effective constitutive properties of the cohesive zone as well as in bulk elements. The justification to do so is based on the following hypothesis that *most defects are multiscale entities, so should be the cohesive zone*. Taking crack as an example, except at initial stage and in the atomistic scale, the crack growth is purely a surface separation; once the initial crack starts to grow, it will evolve into a growth of a depleted material layer or zone, which contains voids, grain boundary, slip lines, and surface separations.

* Corresponding author.
E-mail address: shaofan@berkeley.edu (S. Li).

0045-7825/$ - see front matter © 2009 Elsevier B.V. All rights reserved.
doi:10.1016/j.cma.2009.10.008

From the computational perspective, the proposed multiscale cohesive zone model may be viewed as a combination of cohesive finite element and the Cauchy–Born rule method. Tadmor et al. [25] have proposed a quasi-continuum (QC) method as a multiscale simulation method to bridge atomistic simulations and continuum simulations. There are two versions of quasi-continuum methods corresponding to different scales: a local version of QC method applicable at mesoscale and a nonlocal version of QC method that is designated for atomistic scale simulations. However, up to today, how to couple these two versions of the QC method still have many issues, such as the justification of the use of ghost force, etc. Since there is no clear advantage using nonlocal QC method, at least for now, at atomistic scale the preferred simulation tool is still the molecular dynamics (MD) rather than the nonlocal version of QC method, which may be more complicated and costly. The local version of QC method is basically a straightforward application of the Cauchy–Born rule in nonlinear finite element method with linear FE interpolation function, and it is only applicable when material deformation is uniform. In fact, the Cauchy–Born rule has been applied to construct material constitutive relations since 1980s, such as Milstein and Hill [16], Milstein [17], Ericksen [8], Daw and Baskes [5], among others.

The objective of this work is to establish a small scale coarse grained multiscale cohesive zone model that not only has the simplicity of continuum modeling and computation efficiency of finite element methods, but also has the capability of capturing certain particular local non-uniform deformations such as fractures and dislocations. One of the motivations of this research is to seek a possible coarse grained computational micro-mechanics model for simulations of ductile spall fracture at small scales.

The paper is organized in six sections: in Section 2 we shall review both the quasi-continuum method and the finite element Galerkin weak formulation for the conventional cohesive zone model; in Section 3 we shall discuss the construction of the multiscale cohesive zone model; Section 4 is focused on finite element implementation of the cohesive zone model, and in Section 5, a few numerical simulations are presented, and finally in Section 6 we shall discuss some important issues of the multiscale cohesive zone model.

2. Review of existing methods

2.1. Local quasi-continuum method

In the proposed multiscale cohesive zone model, to reduce the computational cost and complexity in computing the atomistic potential energy, the Cauchy–Born rule has been adopted (see Fig. 1) to calculate elastic energy in each element. The so-called Cauchy–Born rule is referring to the following procedure: if the deformation in each element is uniform, the deformation gradient, $\mathbf{F} = \frac{\partial \mathbf{x}}{\partial \mathbf{X}}$, is then constant in each element. Since in a given element $e, e = 1, \ldots, n_{elem}$ the deformation gradient, $\mathbf{F}_e$, is a constant tensor, an arbitrary deformed bond vector $\mathbf{r}_i$ in a unit cell in the element can be found by mapping the corresponding primitive Bravais lattice vector, i.e. the undeformed bond vector $\mathbf{R}_i$, into the deformed vectors,

$$\mathbf{r}_i = \mathbf{F}_e \mathbf{R}_i, \quad i = 1, 2, \ldots, n_b, \tag{2.1}$$

where n_b is the total number of bonds in a unit cell.

On the other hand, because the deformation in each element is uniform, one can compute the elastic energy density in any given element by calculating the potential energy density of an arbitrary unit cell inside the element,

$$W_e = \frac{1}{\Omega_0^b} \sum_{i=1}^{n_b} \phi(r_i) = \sum_{i=1}^{n_b} \phi(\mathbf{F}_e \mathbf{R}_i) = W_e(\mathbf{F}_e), \quad e = 1, 2, \ldots, n_{elem}, \tag{2.2}$$

where Ω_0^b is the volume of the unit cell in the referential configuration, $\phi(r_i)$ is the atomistic potential, $r_i, i = 1, 2, \ldots, n_b$ is the current bond length in a unit cell. Note that the superscript b indicates bulk, and Ω_0^b is the undeformed volume for the unit cell.

Note that the bond vector $\mathbf{r}_i$ is the distance vector between the center atom in the unit cell to one of the atoms at vertex of the unit cell. Taking the hexagonal lattice for example (see Fig. 2), if we only consider the nearest neighbor interaction and assume the equilibrium atomistic bond spacing is a, the six interatomic bond vectors in the undeformed lattice can be expressed as:

$$\begin{aligned}
\mathbf{R}_1 &= (a, 0), \\
\mathbf{R}_2 &= (a \times \cos(\pi/3), a \times \sin(\pi/3)), \\
\mathbf{R}_3 &= (a \times \cos(2\pi/3), a \times \sin(2\pi/3)), \\
\mathbf{R}_4 &= (-a, 0), \\
\mathbf{R}_5 &= (a \times \cos(-2\pi/3), a \times \sin(-2\pi/3)), \\
\mathbf{R}_6 &= (a \times \cos(-\pi/3), a \times \sin(-\pi/3)).
\end{aligned} \tag{2.3}$$

Therefore the deformed bond length is a function of deformation gradient of the element that the unit cell belongs to, i.e. $r_i = |\mathbf{r}_i| = r_i(\mathbf{F})$. Hence, the strain energy density inside each element is a function of the deformation gradient of that element,

$$W_e = \frac{1}{\Omega_0^b} \sum_{i=1}^{n_b} \phi(r_i(\mathbf{F}_e)) = W_e(\mathbf{F}_e). \tag{2.4}$$

Consequently, the constitutive relations for the bulk medium can be established. For instance, the second Piola–Kirchhoff stress can be written in the following form by using the Cauchy–Born rule:

$$\mathbf{S}(\mathbf{C}) = \frac{1}{\Omega_0^b} \sum_{i=1}^{n_b} \phi'(r_i) \frac{\partial r_i}{\partial \mathbf{C}} = \frac{1}{\Omega_0^b} \sum_{i=1}^{n_b} \frac{\partial \phi}{\partial r_i} \frac{\mathbf{R}_i \otimes \mathbf{R}_i}{r_i}, \tag{2.5}$$

where Ω_0^b is the volume of the unit cell in the referential configuration, $\phi(r_i)$ is the atomistic potential, $r_i, i = 1, 2, \ldots, n_b$ is the current bond length for the ith bond in a unit cell, and $\mathbf{C} = \mathbf{F}^T \cdot \mathbf{F}$ is the right Cauchy–Green tensor. Similarly, we can find the first Piola–Kirchhoff stress tensor and Cauchy stress tensor in each element as

$$\mathbf{P} = \mathbf{FS} = \frac{1}{\Omega_0^b} \sum_{i=1}^{n_b} \frac{\partial \phi}{\partial r_i} \frac{\mathbf{r}_i \otimes \mathbf{R}_i}{r_i}, \tag{2.6}$$

$$\boldsymbol{\sigma} = J^{-1} \mathbf{FSF}^T = \frac{1}{\Omega^b} \sum_{i=1}^{n_b} \frac{\partial \phi}{\partial r_i} \frac{\mathbf{r}_i \otimes \mathbf{r}_i}{r_i}. \tag{2.7}$$

Then the strain energy in the element Ω_e can then be written as:

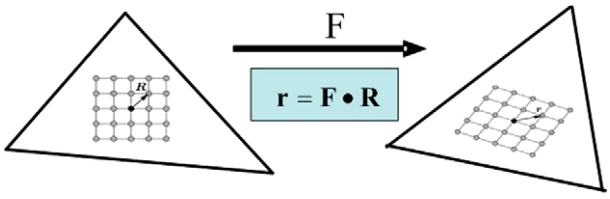

Fig. 1. The Cauchy–Born rule.

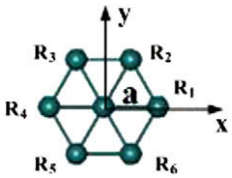

Fig. 2. A hexagonal lattice unit cell.

$$E_e = W(\mathbf{F}_e)\Omega_e \tag{2.8}$$

and the total energy of the system will be,

$$E_{tot} = \sum_{e=1}^{n_{elem}} W(\mathbf{F}_e)\Omega_j. \tag{2.9}$$

This formulation is referred to as the local QC method. The local QC method provides a considerable computational simplification in evaluation of elastic energy of a quasi-continuum system, when surface and interface energies may not be important. For solids containing defects, the deformation will then become non-uniform and non-smooth in the vicinity of defects; therefore the assumptions made in local QC are no longer valid.

A nonlocal version of QC has been developed in which the energy is computed using the following ansatz:

$$E_{tot} = \sum_{\alpha=1}^{N_{rep}} n_\alpha E_\alpha(\mathbf{u}_\alpha), \tag{2.10}$$

where n_α is a suitably chosen weight. The energy from each representative atom E_α is computed by visiting its neighboring atoms whose positions are generated using the local deformation. Near defects such as cracks or dislocations, the finite element mesh is also refined to atomic scale to reflect the local deformation more accurately. Practical implementations usually combine both local and nonlocal version of the method.

A main challenge of the quasi-continuum method is how to couple the macroscale local quasi-continuum method with the microscale nonlocal quasi-continuum method. The general nonlocal QC potential energy may lead to some non-physical effects in the transition region. Specifically, taking derivatives of the energy functional to obtain forces on atoms and FE nodes may lead to so-called ghost forces in the transition region, and it has many issues that remain to be resolved, e.g. Shenoy et al. [24] and Miller and Tadmor [15]. The origin of these ghost forces lies precisely in the assumption of locality in the continuum region and the local/nonlocal mismatch in the transition region.

2.2. Cohesive finite element method

Consider a solid subjected to inhomogeneous deformation that is caused by displacement discontinuity as shown in Fig. 3. In engineering applications, this type of strong discontinuities is the characterization of fracture or dislocations. Initially as a single connected domain, Ω_0, the body is broken into two disjointed pieces by a crack. In the referential configuration, the fracture surface, or the plane of division, is denoted as S_0, and it divides the body into two halves: $\Omega_0 = B_0^+ \bigcup B_0^-$. After the deformation $\boldsymbol{\varphi}$,

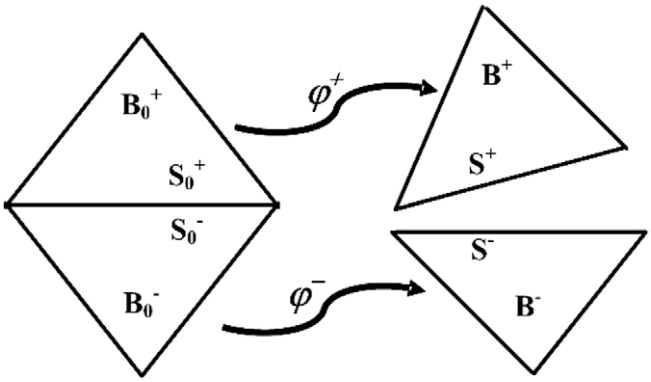

Fig. 3. Illustration of the deformation of cohesive surfaces under finite deformation.

$$\boldsymbol{\varphi} : \Omega_0 \to \Omega;$$

the body arrives at its deformed or current configuration, Ω (see Fig. 3). We use $\mathbf{x}$ denoting the spatial position of a material point $\mathbf{X}$ at the time t, i.e.

$$\mathbf{x} = \boldsymbol{\varphi}(\mathbf{X}) = \mathbf{u} + \mathbf{X}. \tag{2.11}$$

Two crack surfaces now move to S^+ and S^- and the two deformed halves are denoted by B^+ and B^-, respectively. Due to atomic interactions, there will be surface traction between S^+ and S^-.

The strong form of the governing equations of the problem, i.e. the equations of motion, can be written as:

$$\mathrm{DIV}[\mathbf{P}(\boldsymbol{\varphi})] + \rho_0\mathbf{B} = \rho_0\ddot{\boldsymbol{\varphi}} \text{ in } B_0^{\pm}, \tag{2.12}$$

$$\boldsymbol{\varphi} = \bar{\boldsymbol{\varphi}} \text{ on } \partial_\varphi B_0, \tag{2.13}$$

$$\mathbf{P}(\boldsymbol{\varphi}) \cdot \mathcal{N} = \overline{\mathbf{T}} \text{ on } \partial_t B_0, \tag{2.14}$$

$$\mathbf{P}^+ \cdot \mathcal{N}^+ + \mathbf{P}^- \cdot \mathcal{N}^- = 0 \text{ on } S_0^{\pm}, \tag{2.15}$$

where $\mathbf{B}$ is the body force, ρ_0 is the mass density in referential configuration. In above equations, the symbol DIV is the material divergence operator, i.e. $\nabla_{\mathbf{X}}$, $\mathcal{N}$ is the normal vector of surfaces including the cohesive surface, $\overline{\mathbf{T}}$ is the prescribed traction on $\partial_t B_0$. It is assumed that the traction is continuous along the cohesive surface, S_0, see Eq. (2.15). For domain boundaries, it is noted that

$$\partial_\varphi B_0 = \partial_\varphi B_0^+ \bigcup \partial_\varphi B_0^- \text{ and } \partial_t B_0 = \partial_t B_0^+ \bigcup \partial_t B_0^-, \tag{2.16}$$

where $\partial_\varphi B$ is the portion of the boundaries where the displacements are prescribed, and $\partial_t B$ is the portion of the boundaries where the traction is prescribed.

In Eqs. (2.12)–(2.15), $\mathbf{P}(\boldsymbol{\varphi})$ is the first Piola–Kirchhoff stress tensor. Considering the constitutive relation of a hyperelastic material, one may find the first Piola–Kirchhoff stress by differentiating the elastic strain energy density W with respect to deformation gradient,

$$\mathbf{P} = \frac{\partial W}{\partial \mathbf{F}}$$

which clearly indicates that $\mathbf{P}$ is a function of the deformation map, i.e. $\mathbf{P} = \mathbf{P}(\boldsymbol{\varphi})$.

Following standard procedures and neglecting the body force, we can derive the Galerkin weak formulation for Eqs. (2.12)–(2.15) as:

$$\int_{B_0^{\pm}} \rho_0\ddot{\boldsymbol{\varphi}} \cdot \delta\boldsymbol{\varphi} dV + \int_{B_0^{\pm}} \mathbf{P}(\boldsymbol{\varphi}) : \delta\mathbf{F} dV = \int_{\partial_t B_0^{\pm}} \overline{\mathbf{T}} \cdot \delta\boldsymbol{\varphi} dS + \int_{S_0} (\mathbf{P}(\boldsymbol{\varphi}) \cdot \mathcal{N}) \cdot \delta(\boldsymbol{\varphi}^+ - \boldsymbol{\varphi}^-) dS. \tag{2.17}$$

The last term in the above equation is the virtual work done by the cohesive traction force across the plane of discontinuity. If we define the jump there as:

$$\boldsymbol{\Delta} = \boldsymbol{\varphi}^+ - \boldsymbol{\varphi}^- \tag{2.18}$$

then we can re-write the last term as:

$$\int_{S_0} (\mathbf{P}(\boldsymbol{\varphi}) \cdot \mathcal{N}) \cdot \delta(\boldsymbol{\varphi}^+ - \boldsymbol{\varphi}^-) dS = \int_{S_0} \mathbf{T}^{cohe} \cdot \delta\boldsymbol{\Delta} dS, \tag{2.19}$$

where $\mathbf{T}^{cohe}$ denotes the cohesive traction. In continuum cohesive theory, it is defined through the cohesive law:

$$\mathbf{T}^{cohe} = \frac{\partial W^s}{\partial \boldsymbol{\Delta}}, \tag{2.20}$$

where W^s is the surface energy density.

In continuum cohesive FEM theory, W^s is *empirical*, and the cohesive element between two bulk elements is in fact a virtual entity, by which we mean that the interface element has no vol-

ume or area associated with it. Once W^s is being prescribed, one can calculate cohesive traction along the element boundary and subsequently find the cohesive force contribution to each nodal degree of freedom. However, a caveat for continuum cohesive zone model is that one has to make an extra effort to choose a cohesive surface potential, so that it is consistent with the constitutive relations in the bulk material, if one wishes to obtain simulation result that can be compared with experimental tests. Ultimately, one will have to justify one's choice. Many times, some choices just cannot be justified because of the complex size effects at small scale.

In a quasi-continuum medium, the properties of the bulk material are determined by the atomistic potential in a coarse graining procedure. To be true to the spirit of coarse graining, we believe that the effective interface cohesive relations should be also derived based on the same coarse graining procedure as in the bulk material.

The essential difficulty to do so appears to be the discontinuity as a form of local inhomogeneous deformation, because it makes the Cauchy–Born rule break down and hence the coarse graining scheme. To resolve this issue, we need to modify the *bulk* Cauchy–Born rule to incorporate or to accommodate kinematics of strong discontinuity. In other words, we need to construct a general non-uniform deformation field that can accommodate *strong discontinuity*, so that we can extend the local quasi-continuum FEM formulation to situations where the strong discontinuity is present.

3. A multiscale cohesive zone model for quasi-continua

In this work, we shall use the Cauchy–Born rule (see Fig. 1) to establish the constitutive relation for the bulk medium, and this will provide us an atomistically based macroscale constitutive relation in multiscale computations. On the other hand, by doing so we implicitly assume that the local deformation is uniform, which will prevent us to simulate highly non-uniform deformations such as dynamic fracture.

In order to represent possible non-uniform local deformation fields caused by the presence of defects, we first remodel or re-construct the material interface as a finite width compliance cohesive zone, which is the weakest link in an otherwise homogeneous medium (see Ibach [11]). In Fig. 4, it shows that the cohesive zone between two bulk media is remodeled as a different lattice strip region whose lattice constants and atomistic potential are different from those of the bulk medium. We assume that a locally non-uniform deformation field may be represented by a *piece-wise uniform deformation field* that employs a finite width cohesive zone to connect uniformly deformed bulk elements, and we further assume that the non-uniform local deformation is mainly confined in the cohesive zone. To quantitatively deal with the non-uniform deformation inside the finite-width cohesive zone, we then assume that the non-uniform deformation is multiscale in character, and its overall (average) deformation at the scale of the bulk element size can be expressed as an affine deformation. For example, in the case of plane strain, it reads as follows:

$$\bar{x}_1 = a_1 + \overline{F}^c_{11} X_1 + \overline{F}^c_{12} X_2, \tag{3.1}$$

$$\bar{x}_2 = a_2 + \overline{F}^c_{21} X_1 + \overline{F}^c_{22} X_2, \tag{3.2}$$

$$\bar{x}_3 = a_3 + X_3, \tag{3.3}$$

where $\overline{F}^c_{ij}$ are constants. Here the main argument is that the non-uniform deformation field is mainly confined inside the cohesive zone between the adjacent bulk elements, and its effective or overall displacement field can be treated as an affine displacement field, Eqs. (3.1)–(3.3). In other words, the effective affine displacement field inside the cohesive zone is a coarse grain model for local non-uniform displacement field. Therefore in the proposed multiscale cohesive zone model, we are making two coarse graining models: one for the bulk medium and one for the material interfaces, or defects. To compare the difference in kinematics between the conventional cohesive zone model and the multiscale cohesive zone model proposed in this work, we juxtapose their local deformation maps in Fig. 5.

In two-dimensional finite element discretization, the multiscale cohesive zone model may be simplified as two triangle bulk elements sandwiching one quadrilateral cohesive element (see Fig. 6). The beauty of such coarse graining procedure is that the effective deformation field can be uniquely determined by the bulk finite element nodal displacements, and the coarse grain model for the cohesive zone is properly connected with the kinematics of bulk elements that are treated as a quasi-continuum. Consider the 2D plane strain case, and fix the rigid body motion $a_1 = a_2 = a_3 = 0$. One can easily determine the effective deformation gradient $\overline{\mathbf{F}}^c$ by using the information of FEM nodal displacements. For example, we can use the deformations of two diagonal lines of the cohesive zone, which can be expressed by the four FEM nodal displacements, to explicitly determine effective deformation gradient $\overline{\mathbf{F}}^c$ inside the cohesive zone as follows (see Fig. 7):

$$\begin{bmatrix} \overline{F}^c_{11} \\ \overline{F}^c_{12} \\ \overline{F}^c_{21} \\ \overline{F}^c_{22} \end{bmatrix} = \frac{1}{(ad-cb)} \begin{bmatrix} d & 0 & -b & 0 \\ -c & 0 & a & 0 \\ 0 & d & 0 & -b \\ 0 & -c & 0 & a \end{bmatrix} \begin{bmatrix} x^+_{\ell+1} - x^-_{\ell} \\ y^+_{\ell+1} - y^-_{\ell} \\ x^+_{\ell} - x^-_{\ell+1} \\ y^+_{\ell} - x^-_{\ell+1} \end{bmatrix}, \tag{3.4}$$

where $a = X^+_{\ell+1} - X^-_{\ell}, b = Y^+_{\ell+1} - Y^-_{\ell}, c = X^+_{\ell} - X^-_{\ell+1}, d = Y^+_{\ell} - Y^-_{\ell+1}$.

Previously without the coarse graining interface model, the local QC method can only provide a coarse grained model for bulk materials; that is why it cannot solve small scale defect evolution problems. By constructing a finite width cohesive network, the multiscale cohesive zone model can at least represent the overall non-uniform deformation caused by defect evolution. The next question is:

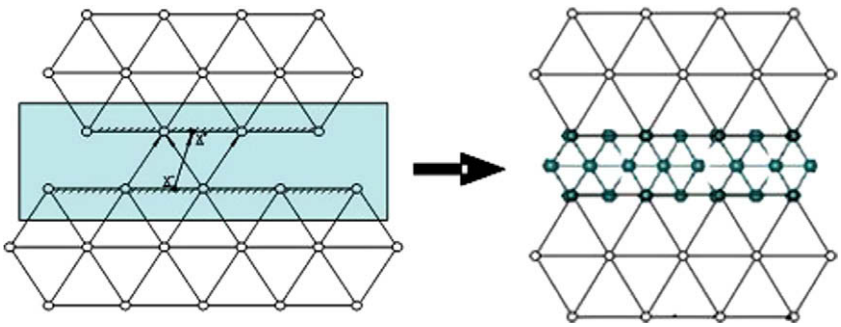

Fig. 4. Reconstruction of cohesive interface – an atomistic cohesive zone model.

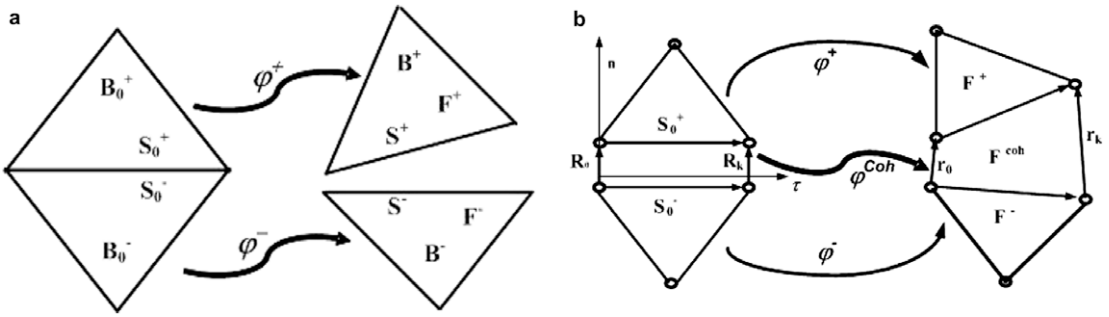

Fig. 5. Comparison of kinematics between (a) conventional cohesive zone model and (b) the multiscale cohesive zone model.

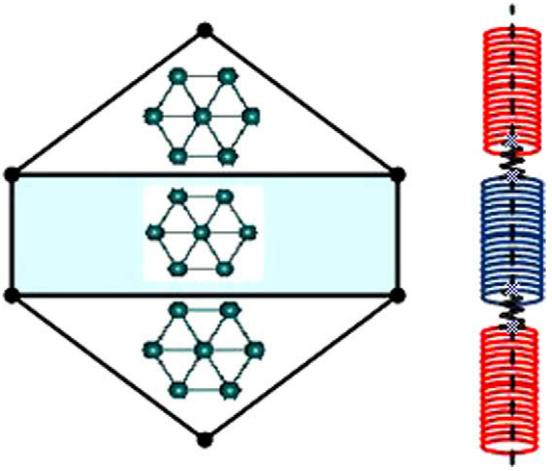

Fig. 6. Illustration of the cohesive zone model.

how do we construct cohesive laws for a weak interface zone?

To answer this question, we first exam the constitutive relations for realistic weak interfaces, for instance, the grain boundary. The cohesive laws in the grain boundary have been studied by Rice [21] and Rice and Beltz [22] as what is called the Rice–Peierls approach. In fact, the essence of the Rice–Peierls approach is similar to the basic idea of the depletion potential in colloidal physics. The nature of the cohesive force inside the grain boundary may be considered as the colloidal adhesive force, and it can be obtained by various coarse graining methods. This motivates us to apply the Derjaguin approximation [6] to find the cohesive potential inside the cohesive zone. Since we consider the cohesive zone as a physical zone with dimension, we can then apply the local version of quasi-continuum method to the cohesive zone to obtain a coarse grained stress–strain relation for the cohesive zone region. That is, we can obtain the constitutive relations for both bulk region and cohesive element by employing the same local version of quasi-continuum method. For instance, the first Piola–Kirchhoff stress inside the cohesive zone can be written as:

$$\mathbf{P} = \frac{\beta_c}{\Omega_0^c} \sum_{i=1}^{n_b} \frac{\partial \phi_{cohe}}{\partial r_i} \frac{\mathbf{r}_i \otimes \mathbf{R}_i}{r_i}, \tag{3.5}$$

where Ω_0^c is the volume of a unit cell inside the cohesive zone, and ϕ_{cohe} is the so-called depletion potential inside the cohesive zone. Even though for some realistic interfaces, there may be no definite lattice structure with atomistic resolution. However, there exist long range order structures or interface structures that come from surface or interface remodelings. In the spirits of homogenization, we assign *an equivalent defect lattice structure* to each cohesive interface, and β_c is the adjustable factor for equivalent cohesive zone lattice density.

The key here is how to obtain the depletion potential as well as the related "equivalent interface lattice" constants for given cohesive zone. To do so, we first assume that the cohesive zone region has a finite thickness R_0. The width of the cohesive zone, R_0, is a physical parameter that is related to the characteristic length scale of specific defects considered. In this study, we choose $10^{-3}|S_0^{\pm}| \leqslant R_0 \leqslant 10^{-1}|S_0^{\pm}|$, and $S_0^{\pm}$ are the length of the sides of the adjacent bulk elements. The lower limit aspect ratio is a restriction limit beyond which numerical ill-conditioning may happen in computations. The upper limit aspect ratio may limit how much refinement we can do, as the mesh size approaches to atomistic scale, because R_0 has to be greater than 4–5 lattice spacings in order to apply the Cauchy–Born rule to the effective displacement field in the cohesive zone.

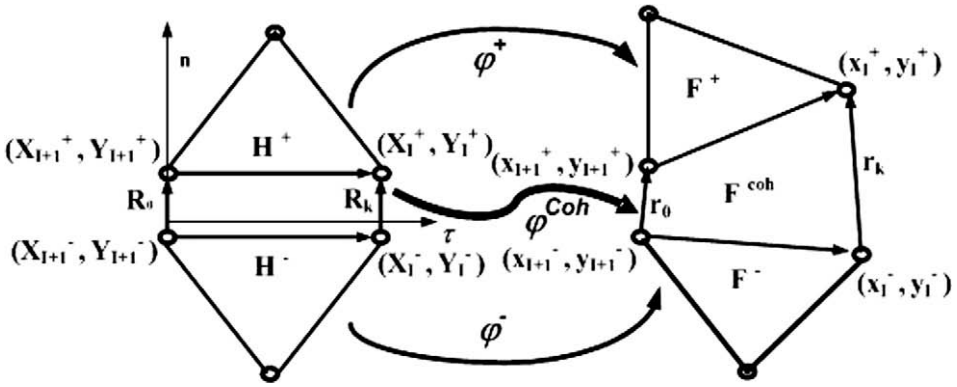

Fig. 7. Deformation gradient in cohesive zone.

To obtain the depletion potential in the cohesive zone, we assume that the cohesive zone is a compliance interface, and it is much weaker than the adjacent bulk elements, and the intermolecular interaction inside the cohesive zone is a type of the Van der Waals interaction between non-covalent bonds or quasi-covalent bonds. The cohesive strength of the cohesive zone can then be determined by the intermolecular forces in surrounding the bulk medium. Under these assumptions, when we calculate the interaction between two material points inside the cohesive zone and the bulk medium, we may consider that the bulk medium is rigid with almost no deformation, so the two bulk elements adjacent to the compliant cohesive zone may be viewed as two rigid body half spaces (see Fig. 8). If the atomistic potential for a given bulk medium is available, which can be a pair potential or EAM (embedded atom method) potentials (Daw and Baskes [5]), we can obtain the atomistic potential of the cohesive zone by integrating the bulk potential over the rigid bulk medium half space.

For instance, if the Lennard-Jones (LJ) potential is chosen as the bulk potential shown in Eq. (3.7), a coarse graining interface potential can be obtained by analytical integration (see Israelachvili [12]),

$$\phi_{cohesive}(r) = \int_{\text{Half Space}} \beta\phi_{bulk}(r - r')dV', \tag{3.6}$$

where β is the atomic density. The interface depletion potential may have close form expressions, if we consider pair potentials. For example, if we consider that the atomistic potential inside the bulk material is the LJ potential,

$$\phi_{bulk} = 4\epsilon\left(\left(\frac{\sigma}{r}\right)^{12} - \left(\frac{\sigma}{r}\right)^{6}\right) \tag{3.7}$$

the interface depletion potential will be

$$\phi_{cohesive} = \frac{\pi\epsilon}{\sqrt{2}}\left(\frac{1}{45}\left(\frac{r_0}{r}\right)^{9} - \frac{1}{3}\left(\frac{r_0}{r}\right)^{3}\right), \tag{3.8}$$

where ϵ is the depth of the potential well, and σ is the (finite) distance at which the bulk atomistic potential is zero. $r_0 = \sigma 2^{1/6}$ is the equilibrium bond distance in the bulk material. The above potential has also been used by the present authors in computational adhesion mechanics e.g. Sauer and Li [23].

Now in the multiscale cohesive zone model, the cohesive zone is constitutively consistent with the bulk material. In Fig. 9, we compare the force–displacement relations of the bulk medium (red lines) with that of the cohesive zone (blue lines). To demonstrate why the multiscale cohesive zone model works, one may simplify the 2D bulk-cohesive zone sandwich as an one-dimensional three spring model, in which three springs are in series connections; two red springs representing two bulk elements are at top and bottom and one blue spring representing the cohesive interface is in the middle of the series connections (see Fig. 6). Among all three springs, the tensile force should be equal due to the series connections. Therefore as the tensile force increases the displacements in both bulk medium and cohesive zone will increases until the force in cohesive zone reaches to its maximum. After the cohesive force in the cohesive zone reaches to maximum, it will unload as the displacement inside the cohesive zone increases, which will eventually lead to surface separation, whereas in the bulk region, the force and displacement will be restricted in the dark color region, which is almost a linear elastic relation, and the magnitude of displacement field in the bulk (red spring) is limited in a very small range. In Fig. 10(a), we plot the normal traction against normal separation distance from our simulation results, it is observed that as expected the normal traction shows a similar pattern as the interatomic force as shown in Fig. 9. In Fig. 10(b), we plot the tangential traction against tangential separation distance.

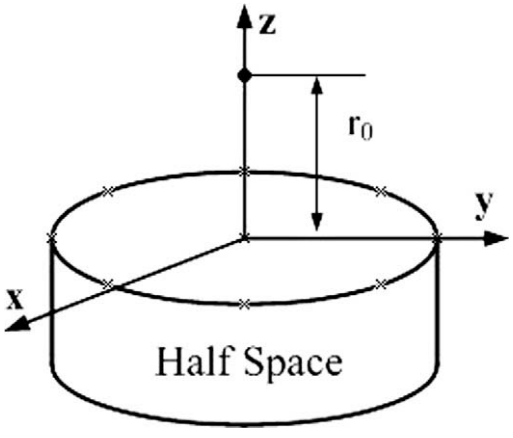

Fig. 8. Integration scheme for acquiring cohesive zone depletion potential.

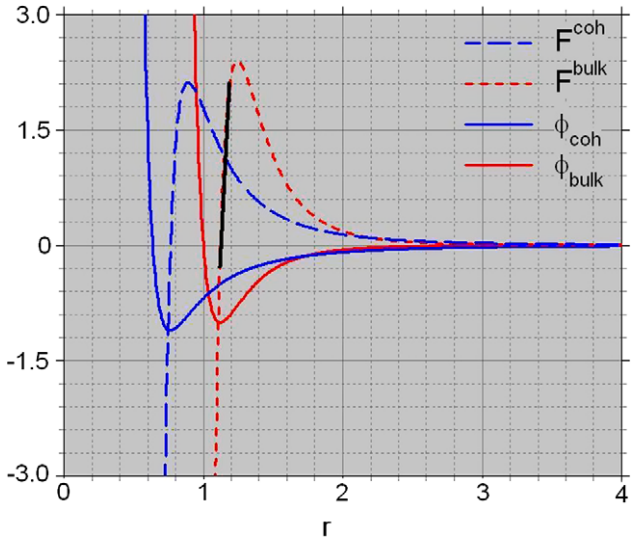

Fig. 9. Comparison between bulk zone and cohesive zone force–displacement relations.

Remark 3.1. Zhou and Huang [28] have pointed out that it is not necessary that an interface is always softer than the bulk materials. Whether a particular surface is softer or stiffer depends on the competition between atomic coordination and electron redistribution (which sometimes is referred as bond saturation) on the surface. However, the focus of the present work is the type of surfaces that are formed due to defect evolution. It may be a reasonable assumption that in this case most of cohesive interfaces are softer than the bulk material.

4. FEM Implementations

Once we obtain the stress inside the cohesive zone, we can readily find the cohesive traction forces along the boundaries of adjacent bulk elements as

$$\mathbf{T}^{coh} = \mathbf{P} \cdot \mathcal{N}, \tag{4.1}$$

where $\mathcal{N}$ is the out-normal of adjacent bulk FE elements. Now we can see the advantage of finite-width cohesive zone approach, because it can easily provide cohesive traction along the bulk element boundary without prescribing both normal and tangential cohesive potential separately, which are still difficult to find based on atom-

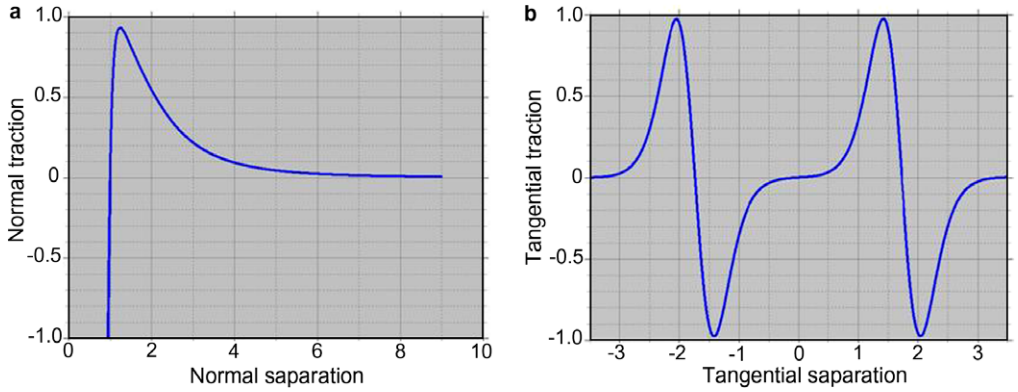

Fig. 10. (a) Cohesive normal traction vs. normal separation distance and (b) tangential traction vs. tangential separation distance in cohesive zone.

istic information. For a given bulk element, the element weak form can be expressed as

$$\int_{B_0^e} \rho_0 \ddot{\boldsymbol{\varphi}}^h \cdot \delta\boldsymbol{\varphi}^h dV + \int_{B_0^e} \mathbf{P}(\boldsymbol{\varphi}) : \delta\mathbf{F}^h dV - \int_{S_c^e} \mathbf{T}^{cohe} \cdot \delta\boldsymbol{\varphi}^h dS = \int_{B_0^e} \mathbf{B} \cdot \delta\boldsymbol{\varphi} dV + \int_{\partial_t B_0^e} \overline{\mathbf{T}} \cdot \delta\boldsymbol{\varphi}^h dS, \quad (4.2)$$

where $\mathbf{B}$ is the body force, B_0^e is the eth element domain, $\partial_t B_0^e$ is the traction boundary of the element, and S_c^e is the cohesive boundary of the element. Notice the subtle differences between Eqs. (4.2) and (2.17). With a finite width cohesive zone, we do not need to define a jump operator any more.

Consider following linear FEM interpolation in each element,

$$\mathbf{u}^h(\mathbf{X}) = \sum_{I=1}^{n_{node}} N_I(\mathbf{X})\mathbf{d}_I. \quad (4.3)$$

Following the standard FE discretization procedure, e.g. Hughes [10], we have the following discrete equations of motion

$$\mathbf{M}\ddot{\mathbf{d}} + \mathbf{f}^{int}(\mathbf{d}) - \mathbf{f}^{cohe}(\mathbf{d}) = \mathbf{f}^{ext}, \quad (4.4)$$

where

$$\mathbf{M} = \mathop{\mathbf{A}}_{e=1}^{n_{elem}} \int_{B_0^e} \rho_0 \mathbf{N}^{eT}\mathbf{N}^e dV, \quad (4.5)$$

$$\mathbf{f}^{int} = \mathop{\mathbf{A}}_{e=1}^{n_{elem}} \int_{B_0^e} \mathbf{B}^{eT}\mathbf{P}^e(\mathbf{d}) dV, \quad (4.6)$$

$$\mathbf{f}^{cohe} = \mathop{\mathbf{A}}_{e=1}^{n_{elem}} \int_{S_c^e} \mathbf{N}^{eT}\mathbf{T}_e^{cohe} dS, \quad (4.7)$$

$$\mathbf{f}^{ext} = \mathop{\mathbf{A}}_{e=1}^{n_{elem}} \left\{ \int_{B_0^e} \mathbf{N}^{eT}\mathbf{B} dV + \int_{\partial_t B_0^e} \mathbf{N}^{eT}\overline{\mathbf{T}}^e dS \right\}, \quad (4.8)$$

where $\boldsymbol{A}$ is the element assemble operator, $\mathbf{N}^e$ is the element shape function matrix, $\mathbf{B}^e$ is the element B-matrix, and $\mathbf{T}$ stands for transpose.

5. Numerical simulations

5.1. Example I: Verification of the cohesive zone model by MD simulations

To validate the proposed multiscale cohesive zone model, we have applied it to simulate a special dynamic fracture process that has been studied in the literature (Buehler et al. [4]). The computation results of the multiscale cohesive zone model is compared with that of the MD simulation conducted by Buehler et al. [4]. The exact problem statement is shown in Fig. 11, in which a 2D

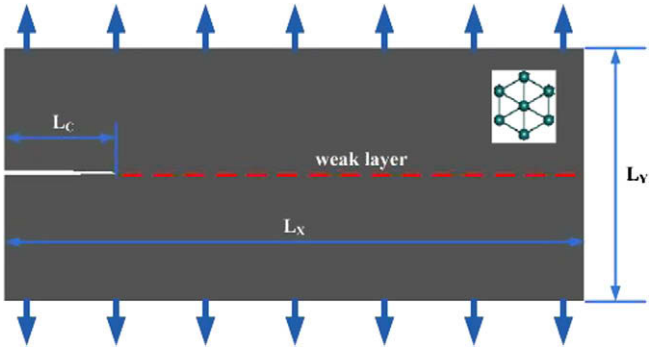

Fig. 11. The simulation domain with lattice orientation and the weak layer.

plate with dimension ($L_X \times L_Y = 8625 \times 3450$ with $L_X/L_Y = 2.5$) is under dynamically prescribed uniaxial tension load. There is a pre-crack at the left side of the plate, and the pre-crack tip is located at ($L_C = L_X/5 = 1725$). Under the dynamic loading, the crack propagates along the horizontal direction (the x direction) in the middle of the plate. For the purpose of comparison, all quantities in these simulations are in reduced units. The specimen size in reduced units is corresponding to micrometer in physical dimensions.

The interfacial lattice is the hexagonal lattice with the equilibrium bond distance $r_1 = 2^{1/6}$, and the crystal orientation is shown in Fig. 11. The lattice orientation inside the cohesive zone is chosen the same as that of the bulk elements. To avoid crack branching, a weak fracture layer is introduced (see Fig. 11) by assuming that the cohesive strength in the rest of the slab are much stronger than the cohesive strength in the weak layer.

We adopt the exact same biharmonic interatomic potential used by Buehler et al. [4], which is composed of two spring constants $k_1 = 36/2^{1/3} \approx 28.57$ and $k_2 = 2k_1$, and it is linearized from the Lennard-Jones (LJ) potential (see Eq. (3.7)):

$$\phi(r) = \begin{cases} \frac{1}{2}k_1(r - r_1)^2, & \text{if } r < r_{on}, \\ a_2 + \frac{1}{2}k_2(r - r_2)^2, & \text{if } r \geqslant r_{on}, \end{cases} \quad (5.1)$$

where $a_2 = \frac{1}{2}k_1(r_{on} - r_1)^2 - \frac{1}{2}k_2(r_{on} - r_2)^2$ and $r_2 = \frac{1}{2}(r_{on} + r_1)$ with $r_{on} = r_1(1 + \varepsilon_{on})$. The parameter r_{on} governs the onset strain (ε_{on}) of the hyperelastic effects.

All the material constants are chosen exactly the same as in Buehler et al.'s simulations, in which Poisson's ratio is chosen as $\nu = 0.33$ for all potentials; The Young's modulus is $E = 33$, and shear modulus $\mu = 12.4$; The density is $\rho \approx 0.9165$ for atomic mass $m = 1$. The shear wave speed is calculated as $c_S = (\mu/\rho)^{1/2} \approx 3.6783$, and the Rayleigh wave speed is calculated

as $c_R \approx 0.9225 c_S \approx 3.3932$. In our simulations, there are 16,000 bulk elements with the characteristic dimension of 20–30 nm, and there are 23,860 cohesive zone elements with the thickness of 5 atomic spacings. In the original model by Buehler et al. [4], there are more than 50 million atoms in their simulations.

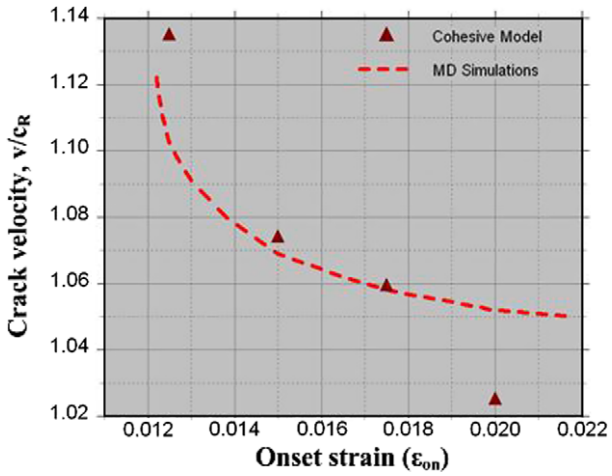

Fig. 12. Comparison of crack speeds between MD simulation and multiscale cohesive zone model simulation.

Constant strain rate ($\dot{\varepsilon} = 1.16 \times 10^{-5}$) is applied over the loading period to strain the system. The Newmark-β integration method (with $\beta = 0$ and $\gamma = 0.5$) has been used in our simulations, and the time step is chosen as $\Delta t = 0.01$. We compute the crack propagation speeds based on the multiscale cohesive zone model under different onset strains, and then we compare our numerical results with the crack speeds obtained from the MD simulations using the same potential and the same material constants (Buehler et al. [4]). The comparison between the results of the multiscale cohesive zone model and that of the MD simulation is shown in Fig. 12. From Fig. 12, one may find that for the mediate value of the onset strains the results obtained by using the multiscale cohesive zone model agrees well with the results obtained by using molecular dynamics.

5.2. Example II: Simulations of crack propagations

After the model verification, we have applied the multiscale cohesive zone model to simulate crack propagations in macroscale. In the simulations, the lattice structure is chosen as the hexagonal lattice showed in Fig. 2, which is different from that of Example I. However, the lattice orientation in the cohesive zone is again the same as that of the bulk elements. We set $\epsilon = 1$ and $\sigma = 1$ for the bulk and cohesive atomistic potentials (see Eqs. (3.7) and (3.8)).

The following is a 2D example of our simulation. Consider a 2D plate (2 mm × 2mm) under unilateral tension (see Fig. 13), and

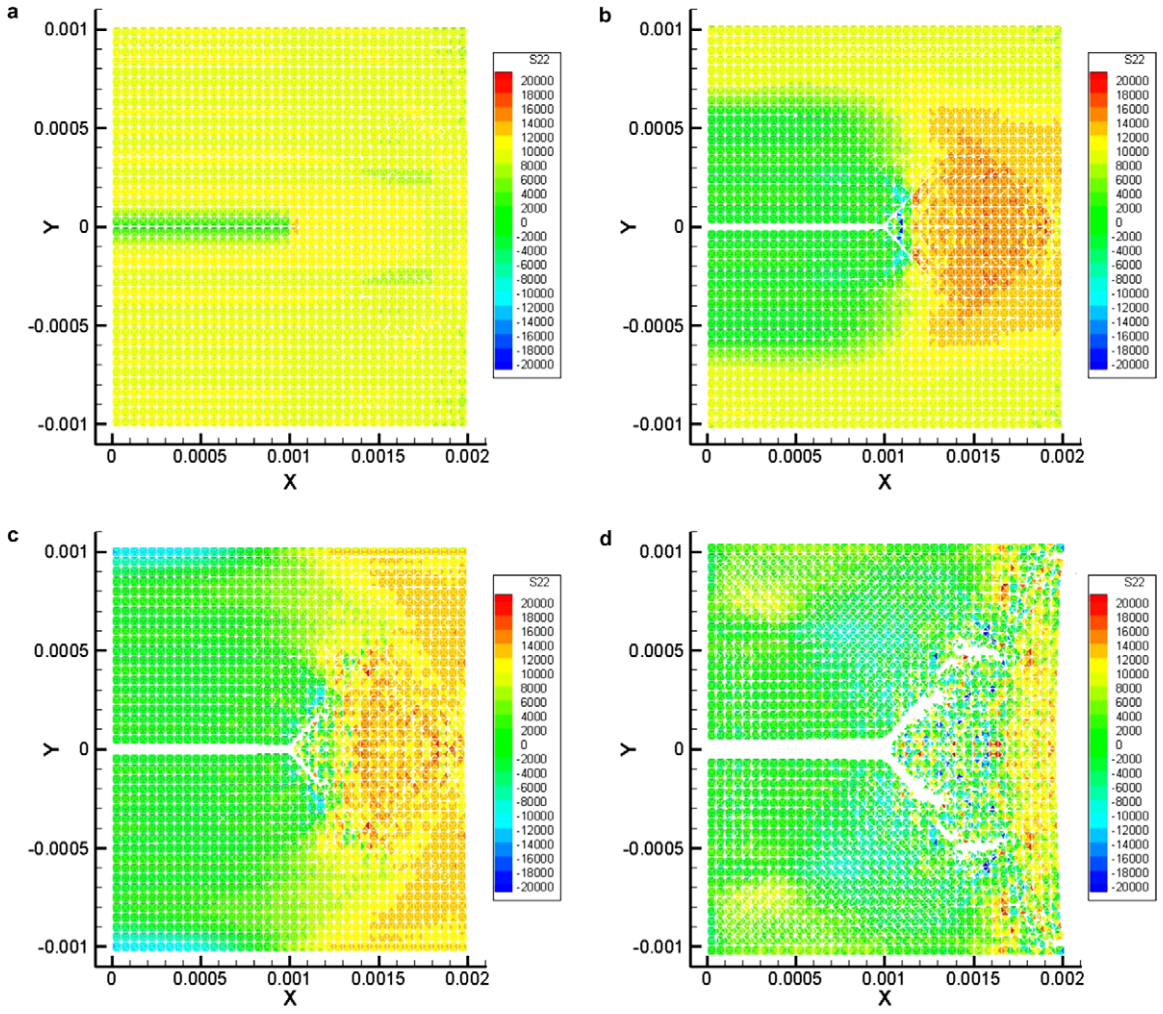

Fig. 13. Stress distribution for crack propagation: (a) $t = 1.25$ μs; (b) $t = 2$ μs; (c) $t = 2.5$ μs; and (d) $t = 4.5$ μs.

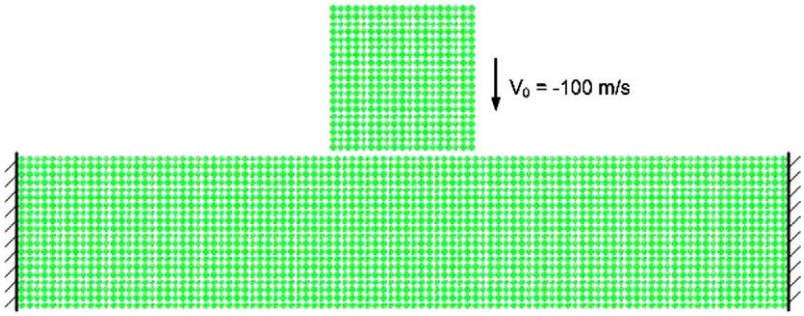

Fig. 14. The statement of the impact problem.

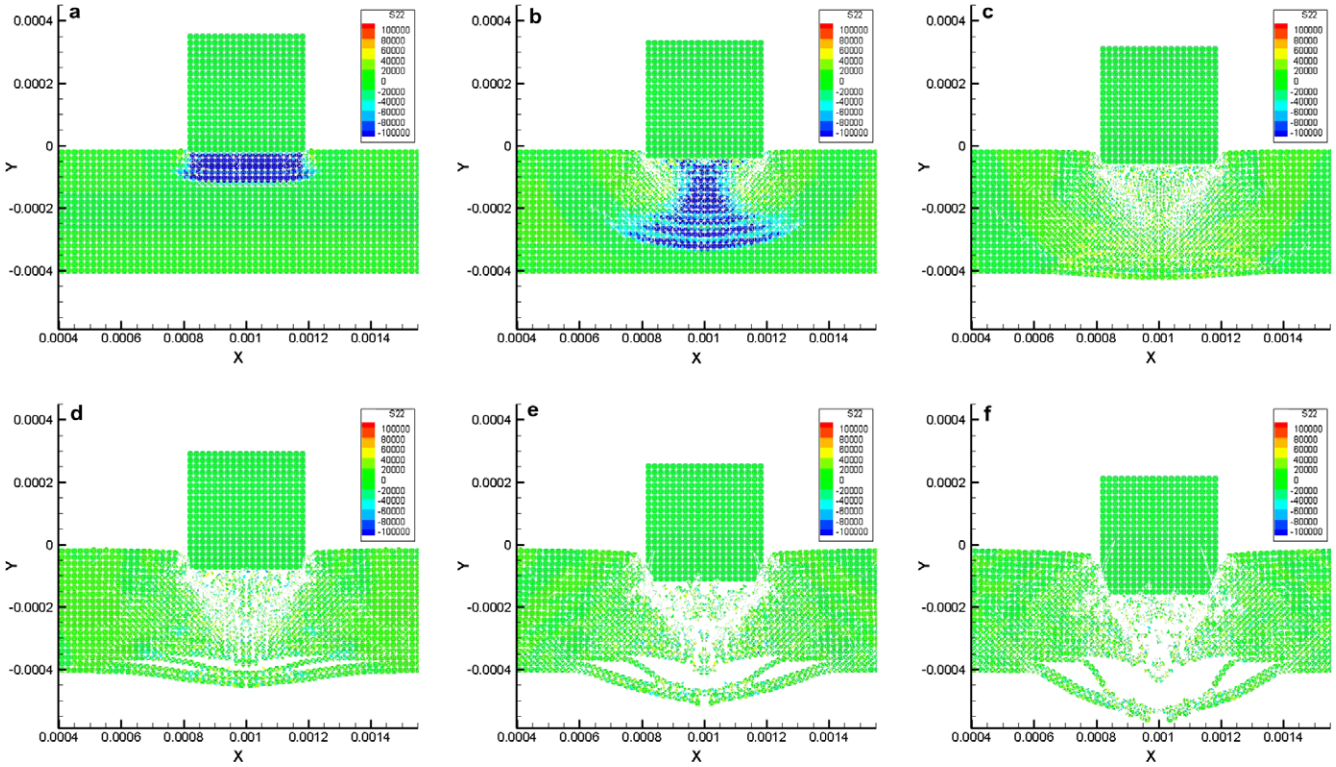

Fig. 15. Snapshots of stress distribution for a contact-impact process: (a) $t = 0.2$ μs; (b) $t = 0.4$ μs; (c) $t = 0.6$ μs; (d) $t = 0.8$ μs; (e) $t = 1.2$ μs; (f) $t = 1.6$ μs.

there is a pre-crack at the left side of the plate. There are totally 9520 cohesive elements and 6400 triangular bulk elements. The time step is chosen as $\Delta t = 1 \times 10^{-10}$ s. The crack branching has been observed from the simulation (see Fig. 13).

5.3. Example III: Simulations of high-speed impact and spall fracture

To further illustrate the versatility of this model, numerical simulations have been carried out to simulate high-speed impact induced spall fractures, which is a very difficult problem that has been elusive to many existing numerical methods (Antoun et al. [1]). The exact problem statement is described in Fig. 14. It is a rigid projectile penetrating a deformable plate. The projectile is a (0.38 mm × 0.38 mm) rigid block with impact velocity $v = 100$ m/s, the target is a (2 mm × 0.4 mm) block clamped at the two ends. In this simulation, there are totally 11,880 cohesive elements and 8000 triangular bulk elements used in the target. The lattice orientations for both the bulk element as well as the cohesive zone are exactly the same as in Example II.

In time integration, the time step is chosen as $\Delta t = 1 \times 10^{-10}$ s. Contact problems are characterized by impenetrability conditions that needs to be enforced during computation. We adopted the exact enforcement of the impenetrability condition in a single time step (see Hughes et al. [9]). The simulation results are shown in Fig. 15. The wave propagation from the contact point to the opposite boundary has been observed. The phenomena of spall fracture under impacts has been captured (see Fig. 15).

6. Discussions

In this paper, we have reported a novel multiscale cohesive zone model, and we have formulated and implemented the multiscale cohesive zone model in the context of finite element method. This method is capable of simulating strong discontinuities across a solid at nanoscale, such as micro-cracks and dislocations at small scales. Compared to the conventional cohesive finite element method, the proposed multiscale cohesive model employs the basic principles of colloidal physics and surface chemistry to determine the interface cohesive force, and it is exploiting the underneath atomistic structure to construct surface or interface cohesive laws. By doing so, the local quasi-continuum formulations has been extended from the interior of the solid to the interfaces,

and it is an approach that yields more accurate results than the conventional cohesive zone approach. This is because first we adopt atomistically enriched constitutive relations, second the normal and tangential potentials are consistent, and third the bulk material properties and the material properties inside the interfacial cohesive zone are consistent. Because of its simplicity, the method is really easy to implemented, and we are currently working on extending the method to 3D problems and problems involving with multiple dislocations.

To be a truly multiscale method, will the multiscale cohesive zone model be able to reach to atomistic resolution? So far the closest case that we have tested is the case in which R_0 equals 5 atomic spacings. Additional technical ingredients may be needed in order to simulate the surface separation in atomistic resolution. However, one of the main advantages of the multiscale cohesive zone model is that this model can be easily incorporated into a con-current multiscale formulation with fine scale physical models such as the molecular dynamics method by using the bridging scale approach e.g. Wagner and Liu [26]. In fact, a con-current coupling between the multiscale cohesive zone model and MD has recently been achieved by the present authors (Li et al. [13]). A multiscale simulation of a moving screw dislocation has been carried out there, which allows a dislocation passing through regions of different scales.

It may be possible that the multiscale cohesive zone model can provide an efficient approximation to calculate cohesive interface stacking fault energy in numerical computations. We are expecting that different interface lattice orientations in the cohesive zone may affect the behaviors of the crack propagation, which may help us explain and simulate brittle/ductile transient in crack propagation. This particular subject is out of the scope of this paper, and it will be further discussed in a separated paper.

Acknowledgements

This work is supported by a grant from NSF (Grant No. CMMI-0800744) and a grant from Army Research Office, which are greatly appreciated.

References

[1] T. Antoun, L. Seaman, D.R. Curran, G.I. Kanel, Spall Fracture (Shock Wave and High Pressure Phenomena), Springer, 2003.
[2] G.I. Barrenblatt, The mathematical theory of equilibrium of cracks in brittle fracture, Adv. Appl. Mech. 7 (1962) 55–129.
[3] A. Braides, A.J. Lew, M. Ortiz, Effective cohesive behavior of layers of interatomic planes, Arch. Rational Mech. Anal. 180 (2006) 151–182.
[4] M.J. Buehler, F.F. Abraham, H. Gao, Hyperelasticity governs dynamic fracture at a critical length scale, Nature 426 (2003) 141–146.
[5] M.S. Daw, M.I. Baskes, Embedded-atom method: derivation and application to impurities, surfaces, and other defects in metals, Phys. Rev. B 29 (1984) 6443–6453.
[6] B.V. Derjaguin, Analysis of friction and adhesion IV. The theory of the adhesion of small particles, Kolloid Z. 69 (1934) 155C164.
[7] D.S. Dugdale, Yielding of steel sheets containing slits, J. Mech. Phys. Solids 8 (1960) 100C104.
[8] J.L. Ericksen, The Cauchy and Born hypotheses for crystals, in: M.E. Gurtin (Ed.), Phase Transformations and Material Instabilities in Solids, Academic Press, 1984, pp. 61–77.
[9] T.J.R. Hughes, R. Talor, J. Sackman, A. Curnier, W. Kamoknukulchai, A finite element method for a class of contact-impact problem, Comput. Methods Appl. Mech. Engrg. 26 (1981) 331–362.
[10] T.J.R. Hughes, The Finite Element Method: Linear Static and Dynamic Finite Element Analysis, Prentice-Hall, 1987.
[11] H. Ibach, The role of surface stress in reconstruction, epitaxial growth and stabilization of mesoscopic structures, Surface Sci. Rep. 29 (1997) 193–263.
[12] J. Israelachvili, Intermolecular and Surface Forces, second ed., Academic Press, 1992.
[13] S. Li, X. Liu, A. Agrawal, A.C. To, The perfectly matched multiscale simulations for discrete systems: extension to multiple dimensions, Phys. Rev. B 74 (2006) 045418.
[14] X. Liu, S. Li, N. Sheng, A cohesive finite element for quasi-continua, Comput. Mech. 42 (2008) 543–553.
[15] R.E. Miller, E.B. Tadmor, The Quasicontinuum method: overview, applications and current directions, J. Comput.-Aided Mater. Des. 9 (2002) 203–239.
[16] F. Milstein, R. Hill, Divergence among the Born and classical stability criteria for cubic crystals under hydrostatic loading, Phys. Rev. Lett. 43 (1979) 1411–1413.
[17] F. Milstein, Crystal elasticity, in: H.G. Hopkins, M.J. Sewell (Eds.), Mechanics of Solids: The Rodney Hill 60th Anniversary Volume, Pergamon Press Ltd., Elmsford, NY, 1982, pp. 417–452.
[18] O. Nguyen, M. Ortiz, Coarse-graining and renormalization of atomistic binding relations and universal macroscopic cohesive behavior, J. Mech. Phys. Solids 50 (2002) 1727–1741.
[19] M. Ortiz, A. Pandolfi, Finite-deformation irreversible cohesive elements for three-dimensional crack-propagation analysis, Int. J. Numer. Methods Engrg. 44 (1999) 1267–1282.
[20] K. Park, G.H. Paulino, J.R. Roesler, A unified potential-based cohesive model of mixed-mode fracture, J. Mech. Phys. Solids 57 (2009) 891–908.
[21] J.R. Rice, Dislocation nucleation from a crack tip. An analysis based on the Peierls concept, J. Mech. Phys. Solids 42 (1992) 239.
[22] J.R. Rice, G.E. Beltz, The activation-energy for dislocation nucleation at a crack, J. Mech. Phys. Solids 42 (2) (1994) 333360.
[23] R. Sauer, S. Li, A contact mechanics model for quasi-continua, Int. J. Numer. Methods Engrg. 71 (2007) 931–962.
[24] V.B. Shenoy, R. Miller, E.B. Tadmor, D. Rodney, R. Phillips, M. Ortiz, An adaptive finite element approach to atomic-scale mechanics – the quasicontinuum method, J. Mech. Phys. Solids 47 (1999) 611–642.
[25] E. Tadmor, M. Ortiz, R. Phillips, Quasicontinuum analysis of defects in solids, Philos. Mag. A 73 (1996) 1529–1563.
[26] G.J. Wagner, W.K. Liu, Coupling of atomic and continuum simulations using a bridging scale decomposition, J. Comput. Phys. 190 (2003) 249–274.
[27] X.-P. Xu, A. Needleman, Numerical simulations of fast crack growth in brittle solids, J. Mech. Phys. Solids 42 (1994) 1397–1434.
[28] L.G. Zhou, H. Huang, Are surface elastically softer or stiffer?, Appl Phys. Lett. 84 (2003) 1940–1942.